INFLUENCE OF A PLASMA ACTUATOR ON AERODYNAMIC FORCES OVER A FLAT PLATE INTERACTING WITH A RAREFIED MACH 2 FLOW

Sandra Coumar [(1)], Romain Joussot [(1)], Jean-Denis Parisse [(2)], Viviana Lago [(1)]

[(1)] *ICARE, CNRS (UPR 3021), 1C Avenue de la Recherche Scientifique, 45071, Orléans cedex 2, France, Email: sandra.coumar@cnrs-orleans.fr*
[(2)] *IUSTI, Aix-Marseille Université / CNRS (UMR 7343), Technopôle de Château-Gombert, 5 rue Enrico Fermi, 13453, Marseille cedex 13, France*

Abstract

Purpose – This paper describes experimental and numerical investigations focused on the shock wave modification induced by a DC glow discharge. The model is a flat plate in a rarefied Mach 2 air flow, equipped with a plasma actuator composed of two electrodes. The natural flow without actuation exhibits a shock wave with a hyperbolic shape. When the discharge is on, the shock wave shape remains hyperbolic but the shock wave is pushed forward, leading to an increase in the shock wave angle. In order to discriminate thermal effects from purely plasma ones, the plasma actuator is then replaced by an heating element.

Design/methodology/approach – The experimental study is carried out with the super/hypersonic wind tunnel MARHy located at the ICARE laboratory in Orléans. The experimental configuration with the heating element is simulated with a code using the 2D full compressible Navier-Stokes equations adapted for the rarefied conditions.

Findings – For heating element temperatures equal to the flat plate wall surface ones with the discharge on, experimental and numerical investigations showed that the shock wave angle was lower with the heating element, only 50% of the values got with the plasma actuator, meaning that purely plasma effects must also be considered to fully explain the flow modifications observed. The results obtained with the numerical simulations are then used to calculate the aerodynamic forces, i.e the drag and the lift. These numerical results are then extrapolated to the plasma actuator case, and it was found that the drag coefficient rises up to 13% when the plasma actuator is used, compared to only 5% with the heating element.

Originality/value – This paper matters in the topic of atmospheric entries where flow control, heat management and aerodynamic forces are of huge importance.

Introduction

In the light of the significant amount of work in the field of flow control with plasma devices, one can consider that it is one of the most booming area in aerodynamics. The reasons are many and varied. Compared to traditional flow control methods, plasma actuators present several advantages like their fast response time, their low weight and size, and the relatively low energy consumption, offering promising applications for flight control systems at high velocities.

The scope of action of plasma-assisted control is wide and promising but it is clear that the expected effects strongly depend on the flow regime. In hypersonic regime or supersonic one, one of the main goals is the control of shock waves with direct applications in spacecraft and supersonic plane flights. One application is related to atmospheric entry missions. Three requirements must be balanced during these missions: deceleration, heating management and accuracy of the localisation and velocity when landing. These requirements strongly depend on drag force which is the dominant force over all others including gravity and lift [1]. The drag force plays a key role because it will influence deceleration, having then a beneficial direct effect on heat loads, vehicle designs and re-entry trajectory. On this purpose, it has been demonstrated that plasma actuators offer the possibility to modify the shock wave shape around the vehicle and thus drag coefficient. One example of plasma flow applications concerns the change in the trajectory of a flying vehicle. The application is about

guided anti-aerial projectiles in which a short plasma discharge is used to deviate the projectile from the initial trajectory [2]. Only few works deal with plasma control applied to supersonic flow and even less when it concerns rarefied flows. [3] have investigated such kind of flow but without clear evidence of plasma actuation even if they observed two distinct discharge modes. [4] have done a very interesting work on the discharge modelling in rarefied regime with external magnetic field conditions but their study is only focused on the discharge modelling without any interaction with a flow. [5] have clearly demonstrated some plasma actuation in a rarefied supersonic flow with a model configuration similar to the cylinder model studied by the FAST team [6]. Nevertheless, in such case, the boundary layer interaction is different to the one occurring in the present work. [7] present an interesting study on a test case quite close to the flat plate test case but without really investigating the non thermal effect due to the plasma.

This paper presents a joined and coupled effort between a modeling and numerical simulation from the IUSTI laboratory in Marseille and experiments carried out at ICARE, a CNRS laboratory located at Orléans with the experimental platform FAST (Facilities for Aerothermodynamics and Supersonic Technologies). In order to have a deep understanding of physical phenomena, that kind of approach is almost mandatory in a multiphysics problem like plasma flow control. The experiments are used to validate the modeling and the numerical codes and the simulations give access to data that could not be measured. In this case this methodology is used to calculate aerodynamic forces: lift and drag.

Experimental setup

The MARHy wind tunnel

The MARHy low density facility belongs to the platform FAST located in the ICARE laboratory (CNRS). This wind tunnel was formerly known as SR3 of the Aerothermics Laboratory and is used for both academic and industrial research. A schematic view of the facility is presented in Figure 1. When supplied with different nozzles, the wind tunnel generates flows from Mach 0.8 to Mach 21 and covers a large range of Reynolds numbers from 10^2 up to 10^5, calculated with a reference length of 10 cm. The present study was carried out with a Mach 2 contoured nozzle, giving a uniform air flow distribution through the test section with a core of 12 cm in diameter [8]. Table 1 indicates stagnation and free-stream conditions corresponding to a geometric altitude of 67 km according to the US Standard Atmosphere, 1976.

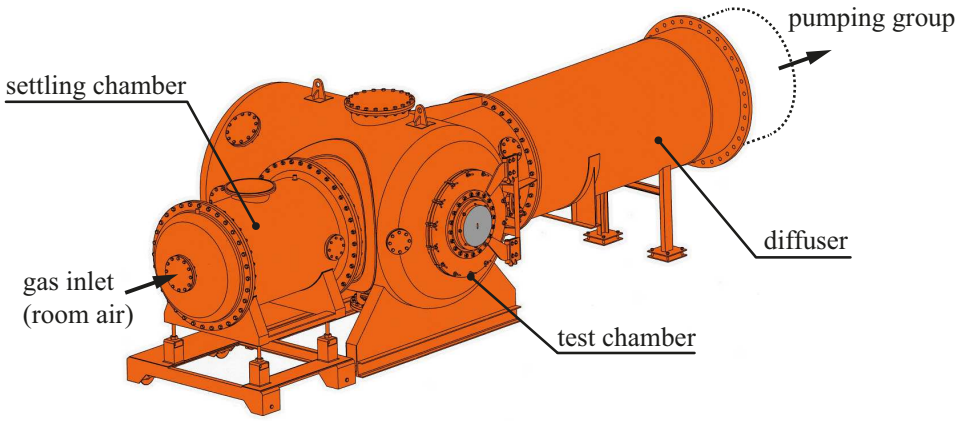

Figure 1. Schematic view of the MARHy wind tunnel.

Table 1. Operating conditions.

Stagnation conditions	Free stream conditions
p_0 = 63 Pa	p_1 = 8 Pa
T_0 = 293 K	T_1 = 163 K
$\rho_0 = 7.44 \times 10^{-4}$ kg·m^{-3}	$\rho_1 = 1.71 \times 10^{-4}$ kg·m^{-3}
	$\mu_1 = 1.10 \times 10^{-5}$ Pa·s
	U_1 = 511 m·s^{-1}
	M_1 = 2
	λ_1 = 0.260 mm
	$q_m = 3.34 \times 10^{-3}$ kg·s^{-1}

Flat plate and actuators

The model under investigation is a flat plate (100 mm-long, 80 mm-wide and 4 mm-thick) made of quartz with a sharp leading edge (15°). The flat plate is placed in the test section, 174 mm downstream the nozzle exit (see Figure 2). The Reynolds number based on the flat plate length L is calculated with the relation $Re = U_1 L/\nu 1$, where U_1 is the free stream velocity and ν_1 is the cinematic viscosity. According to the experimental inflow conditions, this Reynolds number is about 794. The Knudsen number ($Kn = \lambda_1/L$), based on the same experimental conditions, is $Kn = 0.003$, corresponding to the slip-flow regime or slightly rarefied regime [9].

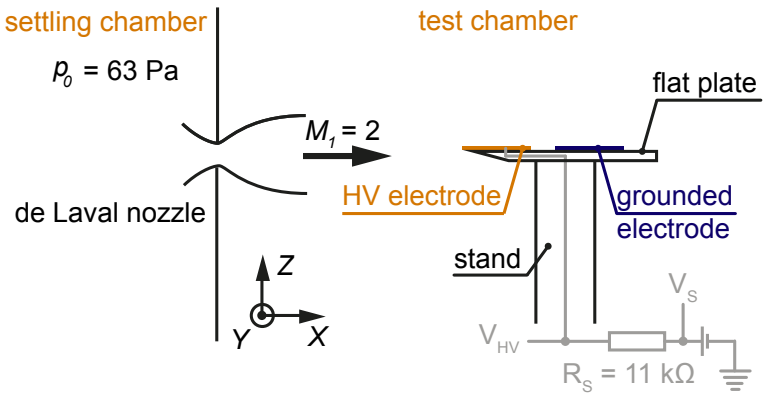

Figure 2. Flat plate equipped with the plasma actuator.

The plasma actuator is composed of two aluminum electrodes (80 mm-long, 35 mm-wide, 80 µm-thick), flush mounted on the upper surface of the flat plate (see Figure 3*a*). The first electrode, called the active electrode or the cathode, is set at the leading edge of the plate, and is connected to a high voltage DC power supply (Spellman, SR15PN6) through a resistor (R_s = 11 kΩ), while the second electrode is grounded. The high voltage V_s is fixed with the power supply, which delivers the discharge current I_{HV}. The voltage applied to the active electrode, V_{HV}, is then calculated with the following relation: $V_{HV} = V_s - R_s I_{HV}$. V_s and I_{HV} are read directly on the power supply. This procedure ensures the stability of the discharge conditions.

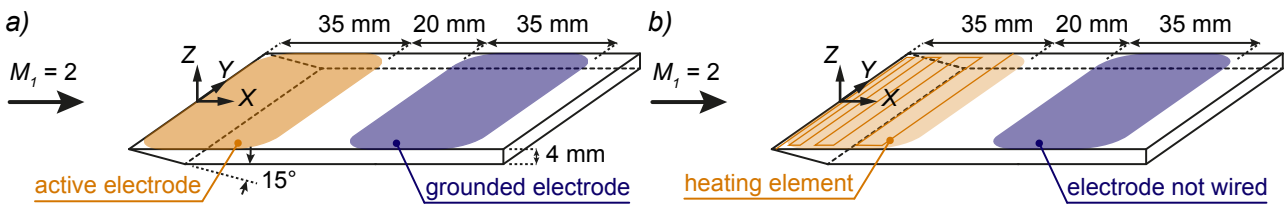

Figure 3. Schematic views of the flat plate with: a) the plasma actuator and b) the heating element.

In order to estimate the surface heat effect only produced by the plasma actuator, a heating element is used as actuator. The heating actuator, namely the heater, is composed of a 0.15 mm-diameter resistance wire

(28 Ω.m^{-1}, Cu-Ni-Mn alloy) embedded between two layers of polyimide film. The heater replaces the active electrode flush mounted on the flat plate surface (see Figure 3*b*). The heating wire is arranged to reproduce an identical heat distribution than the one produced by the active electrode. The heater is powered with a DC power supply (0-60 V, 0-2.5 A).

Average flow field measurements diagnostics

The stagnation and test section pressures are measured with two MKS Baratron capacitance manometers (Type 627D) with 0–10 Torr and 0–0.1 Torr ranges, respectively. Both are connected to a MKS control unit (PR 4000B) with a 12-bit resolution. The total pressure in the flow above the plate is measured with a Pitot probe made of glass in order to avoid electrical interactions with the discharge. According to the probe dimensions and the free-stream flow conditions (see Table 1), it is not necessary to apply rarefaction or viscous corrections to the pressure measurements performed with the Pitot probe [10] and [11]. The Pitot tube is a flat-ended cylinder with an external diameter of D = 6 mm and an internal diameter of d = 4 mm, connected to a MKS Baratron capacitance manometers (Type 626A, 0-1 Torr) linked to a MKS control unit (PDRC-2C).

The polarization of the active electrode produces a glow discharge ionizing the gas flow widely around the flat plate than can be visualized with a PI-MAX Gen-II ICCD camera (1024 $\times$ 1024–pixel array) equipped with a VUV objective lens (94 mm, $f/4.1$). The light is collected through a quartz window located in the wall of the test section chamber. To compare the modified flow field with the baseline defined as the non perturbed flow-field around the flat plate, it was necessary to make visible the base line flow. To this purpose, two copper plates placed on either sides of the flat plate and outside the flow are polarized to create a weak ionization, enough to make possible the detection of the shock with the ICCD camera. This technique, named the luminescent flow visualization technique and described in [12], is employed only for the natural case (i.e., without actuation) or with the heating element.

The evolution of the surface temperature of the flat plate is monitored with an infrared thermography device. The IR device is used to measure the surface during experiments with the plasma actuator or the heater. The IR camera (FLIR ThermaCAM SC 3000) is placed on the top of the wind tunnel and focuses the entire surface of the flat plate through a fluorine window compatible with the IR wavelength range of the camera. The IR camera is equipped with a QWIP-type IR photo-detector composed of a 320 $\times$ 240–pixel array. As the emissivity of the electrodes is low ($\varepsilon < 0.1$ for bare aluminum foil), two black lines are painted on the flat plate surface. For a surface temperature above 335 K, emissivity of the painted electrodes is estimated to be $\varepsilon = 0.84$.

Numerical approach

Investigations involved in this work concern supersonic flows in rarefied regime. Such type of flows can be simulated using Direct Simulation Monte Carlo method, otherwise, some models have been developed in order to adapt classical approaches to cases for which $Kn > 0.001$. As in the present work, where $Kn = 0.003$.
The numerical code was used to reproduce the influence of the heating element on the model, corresponding to the experimental configuration presented in Figure 3*b*. The 2D compressible Navier-Stokes simulations are performed by adapting the boundary conditions in order to match the physical phenomena involved in a rarefied flow regime [13].

Fluid Mechanic Model

Governing equations:

In order to describe the air flow, the 2D full compressible Navier-Stokes equations are used in the conservative form:

- the continuity equation:

$$\frac{\partial \rho}{\partial t} + \frac{\partial \rho u_i}{\partial x_i} = 0, \tag{1}$$

where x_i is the space coordinates, t is the time, ρ is the density and u_i is the velocity in the space direction x_i.

- the momentum conservation equation:

$$\frac{\partial \rho u_j}{\partial t} + \frac{\partial \left(\rho u_j u_i + p\delta_{ij} - \tau_{ij}\right)}{\partial x_i} = 0, \tag{2}$$

where p is the pressure, τ_{ij} the viscous shear stresses tensor and δ_{ij} Kronecker's symbol. It is supposed that the fluid is Newtonian, so the viscous shear stresses tensor can be written as:

$$\tau_{ij} = \mu \left(\frac{\partial u_i}{\partial x_j} + \frac{\partial u_j}{\partial x_i}\right) - \delta_{ij}\frac{2}{3}\mu\frac{\partial u_k}{\partial x_k}, \tag{3}$$

here μ is the viscosity coefficient taken from the JANAF Thermochemical Tables and [14].

- the energy conservation equation:

$$\frac{\partial \rho e_t}{\partial t} + \frac{\partial \left(\rho u_i e_t + u_i p - u_i \tau_{ij} + q_i\right)}{\partial x_i} = 0, \tag{4}$$

where e_t is the total energy $e_t = e + 1/2\rho\Sigma u_i^2$, e is the internal energy, and q_i is the heat flux in the space direction i. The Prandtl number is equal to 0.7, because the experimental gas is air.

Boundary conditions:

Taking into consideration the first-order Knudsen number conditions, the complete slip and the temperature jump at the wall boundary conditions proposed by [15] are used for the equation system (1) – (4) . This choice is made to take into account the rarefaction effects. Considering Knudsen number first order conditions only, the complete slip boundary condition reads:

$$u_s = -\sigma_v \frac{\mu}{p} v_m \left(\frac{\partial u}{\partial y}\right)_w + \sigma_T \frac{\mu}{\rho}\left(\frac{\partial \ln T}{\partial x}\right)_w, \tag{5}$$

where $v_m = \sqrt{2rT_w(x)}$ is the most probable molecular velocity at the surface temperature T_w with $r = \frac{\mathcal{R}}{M_{mol}}$, where $\mathcal{R}$ is the ideal gas constant and M_{mol} the molar mass. σ_v is the slip velocity coefficient and σ_T is the thermal slip coefficient.
In this work, we use the velocity slip coefficient $\sigma_v = 1.012$ given in [15], under the full accommodation assumption. Concerning the thermal slip coefficient σ_T numerous theoretical data are summarized in [16].
In this study the second term in equation (5) is not taken into account because there is one order of magnitude difference compared to the first term even if the surface temperature gradient in the X direction is taken into account. This hypothesis has been validated in previous work [17].

The temperature jump coefficient is based on the diffuse reflection assumption and the Knudsen layer effect. The boundary condition proposed by [15] is chosen for ΔT the temperature jump :

$$\Delta T = -\xi_j^T \frac{\mu}{p} v_m \left(\frac{\partial T}{\partial y}\right)_w, \tag{6}$$

where T_j is the real temperature considering the jump temperature, ξ_j^T is the temperature jump coefficient. For this coefficient, [18] proposed a first expression for ξ_j^T. In this work we use the expression proposed by [15] under diffuse reflection assumption and taking into account the Knudsen layer effect $\xi_T = 1.173\frac{\gamma}{4(\gamma-1)}\frac{\sqrt{\pi}}{Pr}$. Similar values of the temperature jump coefficient were obtained by [19].
Furthermore, the mean free path is usually written as a function of macroscopic parameters:

$$\lambda = k_\lambda \frac{\mu}{p}\sqrt{\mathcal{R}T}, \tag{7}$$

where $k_\lambda = A(\omega) = \frac{2(7-2\omega)(5-2\omega)}{15\sqrt{2\pi}}$ and ω is the temperature exponent of the coefficient of viscosity given by [20] in the variable hard sphere model (VHS).

Numerical Procedure

Numerical scheme:

The numerical code uses a structured grid based on the discretization of the unsteady compressible Navier-Stokes equations by an explicit cell-centered finite volume method. The convective block (Euler) is discretized using a WENO third order accurate TVD-upwind, cell-centered finite volume scheme. The associated Riemann solver comes from [21].
The diffusive block is then discretized with a centered finite difference scheme. The temporal integration is performed by a 2nd order Runge-Kutta procedure.
This code has been validated on numerous test cases and especially for supersonic and hypersonic rarefied flows [22]. In the present work, the numerical code does not use several species and only the macroscopic temperature is considered to describe the flow. Neither the rotational temperature nor the vibrational one is used, meaning that the flow is considered at thermal equilibrium.

Mesh:

The computational domain is divided into three blocks for parallel computing purposes and is uniformly composed by 166,000 cells. The space step is $\Delta x_{min} = \Delta y_{min} = 5.10^{-4}$ m and is chosen as a result of the convergence study but also taking into account that the value of the mean free path in the free stream is $\lambda = 2.7.10^{-4}$ m. The CFL coefficient used to carry out the simulations is 0.75.

Boundary conditions:

The classical boundary conditions are: no reflection or zero gradient ones for the north, east and south, supersonic inflow for the west. For the velocity slip and temperature jump conditions at the wall of the plate, a semi-implicit treatment is used. Unlike previous studies [8], temperature over the flat plate is not constant anymore but is a function of the position X. However, for the case without any discharge, considered as the baseline flow, the temperature is constant and equal to the stagnation temperature of the free stream.

Baseline flow

Experimental study

The flow field around the flat plate is first investigated without any actuation, corresponding to the study of the natural flow (namely, the baseline). The nominal operating conditions of the flow field remain those detailed in Table 1. In this case, the shock wave is experimentally visualized with the luminescent discharge flow visualization technique. Figure 4*a* shows an image of the baseline flow field around the flat plate obtained with the ICCD camera. The air flows from the left to the right. This image results from the averaging and post-processing of 300 snapshots of the flow field recorded with the ICCD camera. The contrast is enhanced with ImageJ software in order to distinguish the shock wave position more precisely than is possible from a single raw image. The contrast of the picture allows to determine the shock wave shape, which can be fitted by an hyperbolic equation. The shock wave angle β is then deduced from the hyperbola asymptote. For each experimental condition, the mathematical analysis is applied to a large number of images in order to average the angle value and estimate the standard deviation.

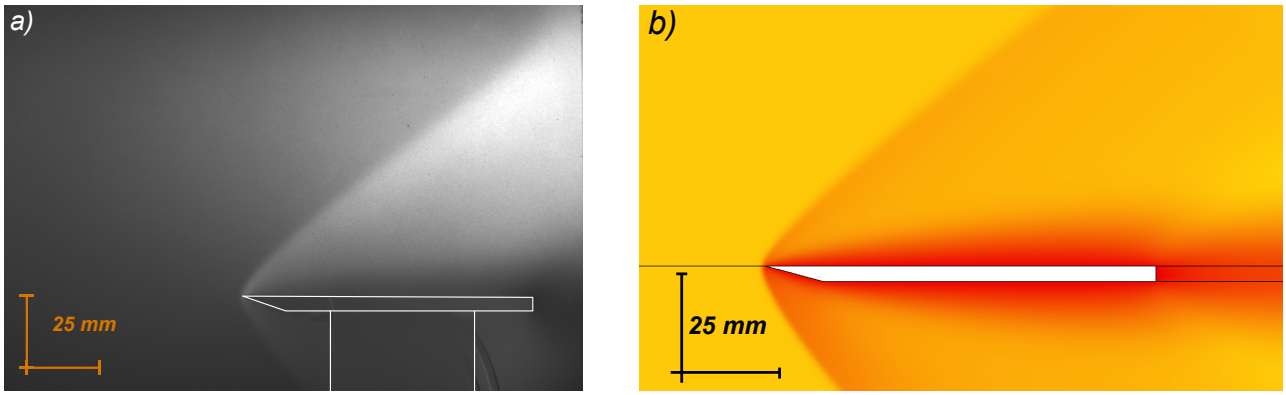

Figure 4. Image of the baseline obtained with: a) the ICCD camera and the luminescent discharge flow visualization technique and b) the numerical simulation.

For the baseline, the value of the shock wave angle is β = 36.4° ± 0.3°. The analysis method is sufficiently sensitive and makes it possible to detect that the shock wave is slightly detached of 1–2 mm from the leading edge of the plate because of the rarefaction effects.

Numerical analysis

The baseline of the Mach 2 flow field is simulated with the numerical code. The input parameters of the numerical simulation are those of the experimental free stream conditions (Table 1). The resulting Mach number flow field is shown in Figure 4*b*. The comparison of the numerical and experimental flow fields shows that the global shape of the shock wave is well reproduced, as well as the stand-off of the shock wave ahead of the leading edge. The longitudinal distribution of the surface temperature is homogeneous with an average value over the flat plate length of 282.8 K. The calculated temperature is therefore slightly lower than the experimental value of 287.4 K. This underestimation of the surface temperature for the simulated baseline can be due to the wall conditions (slip velocity and temperature jump) used to simulate the flow field. For the sake of consistency between the analysis of experimental images and the detection of the shock from the numerical simulations, the same mathematical method was applied and gives a shock wave angle for the simulated baseline of β = 36.7°, which is slightly larger than the experimental value but however, still remains in the range of the experimental shock wave angle measured at β = 36.4° ± 0.3°. This discrepancy is due to a slight overestimation of the shock layer thickness by the numerical code. Figure 5 shows several fields of the baseline: temperature (see figure 5*a*), Mach number (see figure 5*b*), static pressure (see figure 5*c*) and synthetic Pitot pressure (see figure 5*d*) calculated from the dynamic pressure and the flow conditions.

Effect of the plasma actuator on the flow field

The discharge is created by applying a negative DC potential to the active electrode. Figure 6*a* shows the current–voltage (I_{HV}–V_{HV}) characteristic of the plasma actuator. The discharge ignites at the voltage V_{HV} = −0.36 kV and can be sustained down around V_{HV} = −2.5 kV. The discharge current increases with the applied voltage, corresponding to the abnormal glow discharge regime [23]. Over the range of electrical configurations tested with the plasma actuator, the maximum surface temperature $T_{w,max}$ appears to increase with the discharge current (see Figure 6*b*).

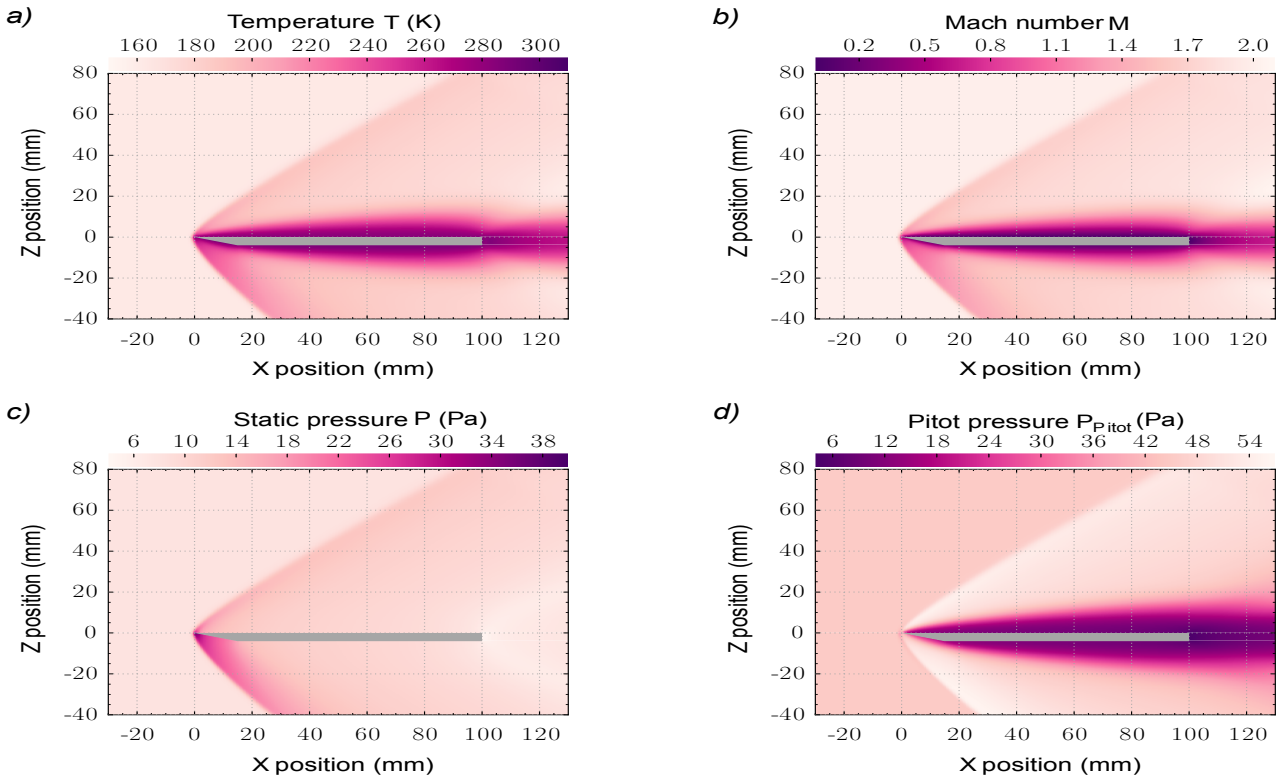

Figure 5. Numerical simulation of the baseline: a) temperature field, b) Mach number field, c) static pressure field, and d) synthetic Pitot pressure field. The free stream Mach number is 2.

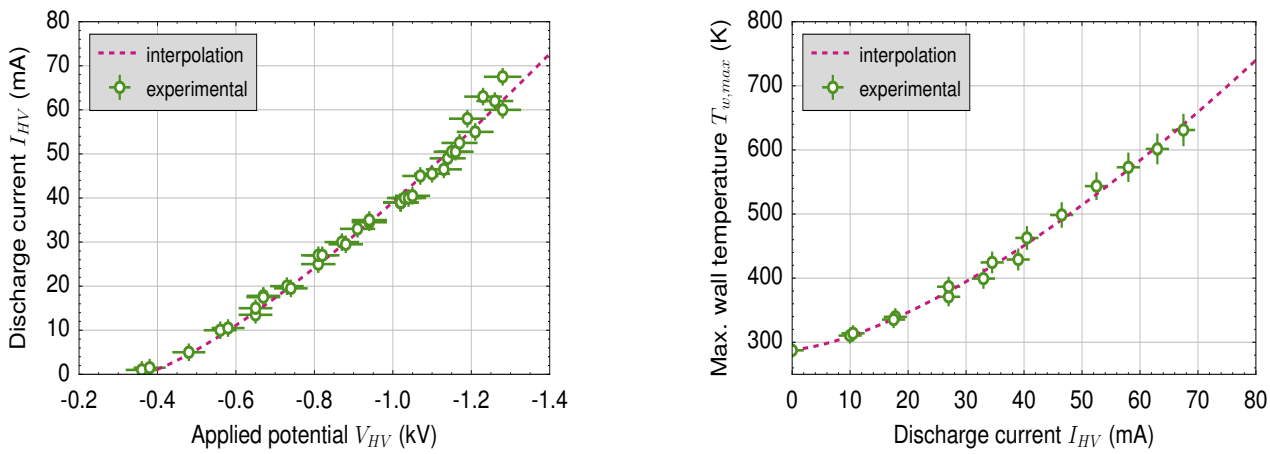

Figure 6. a) Current-voltage characteristic of the plasma actuator and b) Variation of the maximum wall temperature according to the discharge current of the plasma actuator. The free stream Mach number is 2.

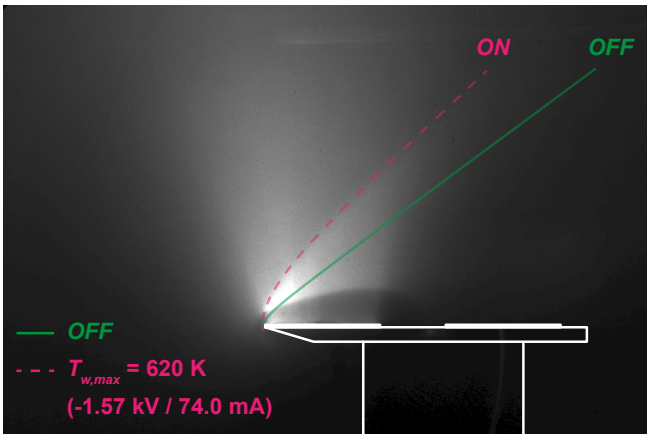

Figure 7. ICCD image of the flow field modified by the plasma actuator. The free stream Mach number is 2.

When the high voltage is switched on, the gas above the cathode is ionized and a plasma (weakly ionized) is created. Visually, it corresponds to the luminous area shown in Figure 7, which exhibits a plume-like shape slightly slanted in the upstream direction. The dark area above the cathode corresponds to the plasma sheath. The plasma discharge induces a modification of the shock wave that is deflected outward from the flat plate surface as illustrated in Figure 7. The shock wave shape of the baseline (solid line) is superimposed on the image. For the electrical configurations experimentally tested, the hyperbolic shape of the shock wave is preserved. In addition, the magnitude order of the shock wave stand-off distance remains within the 1-2 mm-range.

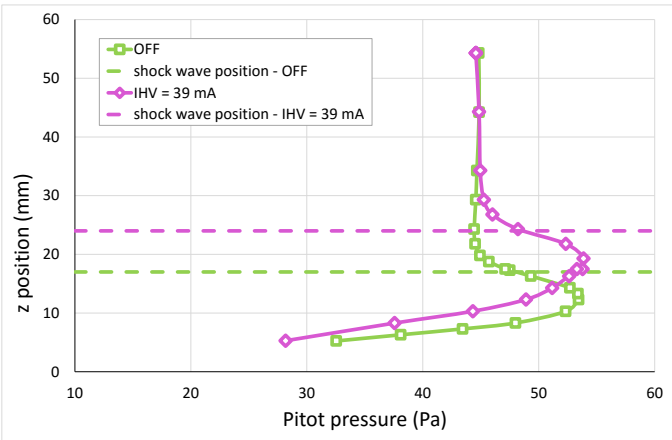

Figure 8. Pitot pressure profiles at x = 17.5 mm and y = 0 mm in the case of the plasma actuator (V_{HV} = −1.47 kV and I_{HV} = 39 mA) with the respective shock positions. The free stream Mach number is 2.

In rarefied flow regimes, one of the main effects expected to be responsible for the shock wave modification is the heating of the model surface [24]. The surface heating induces a displacement effect [25]: the flow viscosity above the heater is modified, inducing an increase in the laminar boundary layer thickness, and, consequently, the shock wave is shifted outward the flat plate surface (i.e., β increases). This effect can be observed more clearly on Figure 8 where two Pitot pressure profiles are presented: one corresponds to the baseline, and the other corresponds to the case when a discharge of I_{HV} = 39 mA is applied. The shape of the profiles measured at x = 17.5 mm (in the middle of the active electrode) shows a knee, typical of the region where the shock wave and the boundary layer are merged. The knee geometry is found at a higher position on the Z-axis, meaning that the thickness of the boundary layer has increased and therefore, the shock wave angle too.

Thermal effects

Experimental study

In order to differentiate the surface thermal effect from other types of effects (for instance, purely-plasma effects, bulk heating effect), experiments are carried out with the heater. In this case, the surface heating of the flat plate induced by the plasma actuator is experimentally reproduced by using the non-uniform heater shown in Figure 3*b*.

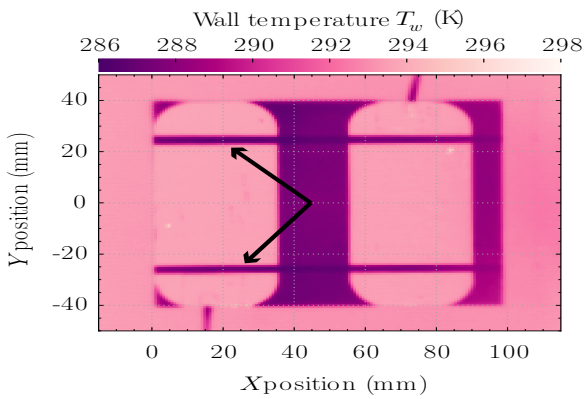

Figure 9. Thermogram of the surface temperature T_w in the case of the baseline. The free stream Mach number is 2.

The longitudinal distributions of T_w are obtained from the thermograms (see Figure 9) for several values of I_{HV}. These distributions follow the two thin black lines painted on the flat plate surface (at y = 25 mm). They show a specific shape and especially a maximum at the position of the active electrode. Figure 10*a* shows a comparison between the temperature distributions measured with the plasma actuator and with the heater. As observed, the heater reproduces accurately the temperature distributions obtained with the plasma actuator. One can notice that the longitudinal distribution of the surface temperature along the flat plate for the baseline (see Figure 10*a* , black dashed line) is homogeneous [26]: T_w is ranged between 286.7 K and 288.8 K with an average value of 287.4 K. Therefore, the shape of T_w distributions are induced by the electric field when the plasma actuator is on and not by the interaction between the flow field and the shock wave.

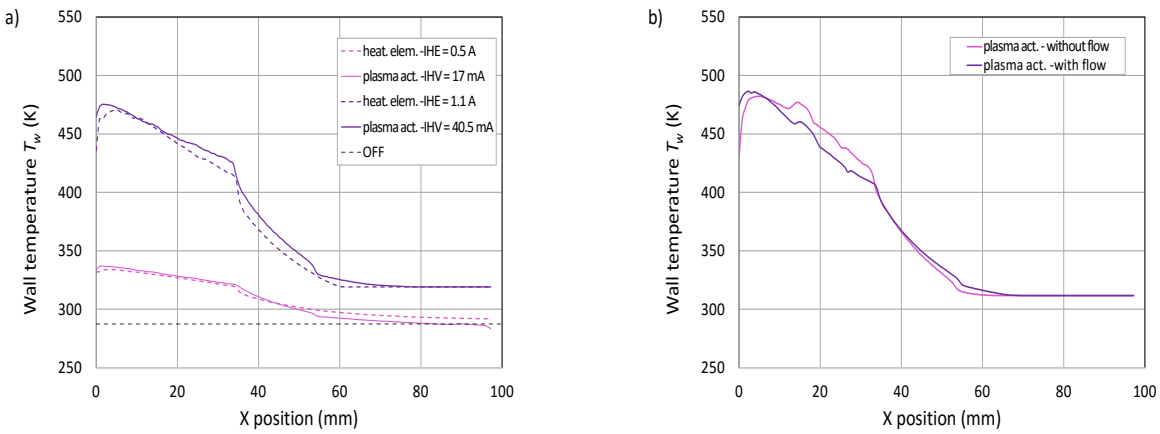

Figure 10. a)Comparison of longitudinal distributions of surface temperature between the plasma actuator (solid lines) and the heating element (dashed lines). The free stream Mach number is 2. And b) Comparison of longitudinal distributions of surface temperature with and without Mach 2 flow for similar power of discharge (P_{HV} = 80 W).

The flat plate surface is heated by applying a DC potential to the heater. The powers of the heater were adapted in order to get the same temperature distributions as with the plasma actuator. A maximum wall temperature up to $T_{w,max} \approx 510\,\mathrm{K}$ can be reproduced with the heater. Higher values of $T_{w,max}$ were not possible to reproduce because of the physical characteristics of the polyimide film (working temperature below 513 K). However, most of the values of $T_{w,max}$ measured with the plasma actuator could be investigated with the heater. When the heating element is used, the purely thermal effect acting on the model surface induces the flow modifications observed.

The heater is made in order to reproduce the surface flat plate temperature T_w measured with the IR camera when the plasma actuator is on. The analysis of the temperature distribution along the flat plate shows that the highest temperatures are measured close to the leading edge above the active electrode where the electric field is the strongest [26]. Downstream the active electrode, the flat plate is heated due to the thermal conductivity of quartz. The lowest temperatures are measured at the trailing edge of the flat plate. The shape of the longitudinal temperature distribution is not due to the interaction between the air flow and the discharge. Measurements have been made with the plasma actuator with the Mach 2 flow and with no flow but at the same static pressure (8 Pa). These measurements are presented on Figure 10*b*, where it can be observed that in both case, the shape of the temperature distribution remain similar.

To analyze the heater effects, images of the flow field are recorded with the ICCD camera once the thermal equilibrium is reached. In the case of the heater, the analysis of ICCD images shows that the thermal effect at the heater surface induces an increase in the shock wave angle although the stand-off distance remains within the 1-2 mm-range for all the operating conditions tested. This result can be observed in Figure 11, where the shock wave angle β is plotted versus the maximum surface temperature $T_{w,max}$. This figure presents the comparison between the measurements performed with both actuators: plasma actuator (open diamonds) and heater (open triangles) and those obtained with the numerical simulations (open circles).
This behavior of the shock angle with the maximum value of the surface plate temperature can be fitted by equation:

$$\beta = a[1 - exp\sqrt[n]{\frac{T_{w,max} - T_w}{c}}] + \beta_0, \tag{8}$$

where $a = 5.89$, $b = 26.14\,\mathrm{mA}$, $\beta_0 = 36.77°$, $n = 1.73$, $c = 128.4$ and $T_{w,max} = 286.6\,\mathrm{K}$ are the best-fit parameters for the plasma actuator.

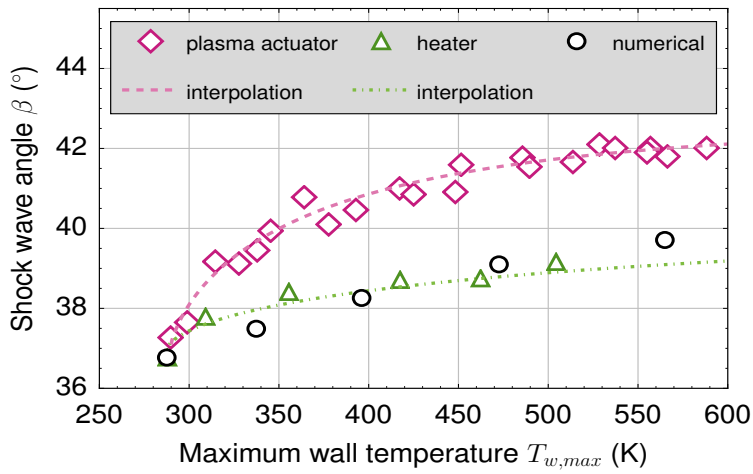

Figure 11. Comparison of the shock wave angles for the different cases studied. The free stream Mach number is 2.

The heating of the flat plate surface accounts for almost half of the total shock wave modification when the plasma actuator is used. However, the contribution of the surface heating on the shock wave modification decreases with the discharge power, meaning that the efficiency of other actuation modes in the shock wave modification increases. Regarding the effects produced by the plasma discharge, one can also consider the

bulk heating of the gas above the flat plate surface. In this respect, temperature measurements above the cathode have been carried out by [27] with optical emission spectroscopy. The results showed that the gas temperature deduced from the rotational temperature is weakly heated by the discharge and therefore, the bulk heating induced by the plasma actuator does not seem to play a significant role in the flow modification.

Numerical analysis

The longitudinal distribution of the surface temperature measured with the IR camera, when the discharge is on, is implemented in the numerical code as the boundary condition for the upper surface temperature of the model. For the rest of the plate and the whole domain, an initial temperature of T_w = 163 K is set.

In order to simulate a Pitot survey of the flow above the flat plate, the synthetic Pitot pressure is calculated from the dynamic pressure and the flow conditions [27]. Figure 12 shows the synthetic Pitot profiles above the flat plate at x = 17.5 mm, for different cases of simulated surface heating. We can notice that the profile shape is slightly different to the ones measured experimentally (see Figure 8). For the numerical simulations, the boundary layer and the shock wave are not merged, suggesting that a shock layer (inviscid flow) is present between the boundary layer and the shock wave because of an inadequate estimation of the wall conditions (slip velocity and temperature jump). However, the numerical simulations confirm our experiments, since the surface heating induces an increase in the boundary layer thickness and, hence, in the shock wave angle.

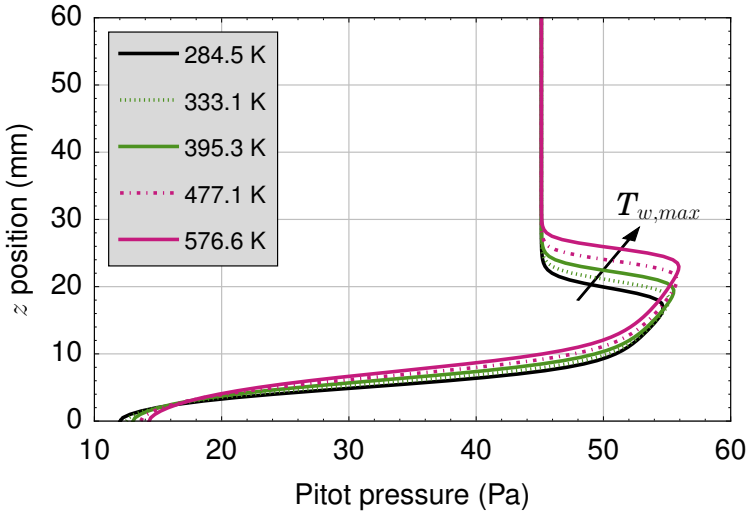

Figure 12. Pitot pressure profiles at x = 17.5 mm in the case of the numerical simulations. The free stream Mach number is 2.

It was shown previously that using the heater instead of the plasma actuator induces similar shock wave modifications: higher the surface temperature is, higher the shock wave angle is [28]. However, for any given value of $T_{w,max}$, the shock wave angle measured with the heater is still lower than the value estimated with the plasma actuator (see Figure 11). This result is supported by the numerical simulations, since they exhibit an increase in β similar to the one measured with the heater.

Calculation of the aerodynamics forces

Calculation method

The pressure distributions along the plate are necessary to calculate the drag and lift forces operating over the model (see Figure 5*c*). As these data are not available experimentally, the numerical simulations are used to calculate the aerodynamic forces. Indeed, with the numerical code, the results give a shape and range of values of the shock wave similar to the experimental results. In particular, the pressure distributions evolve in the same way: they show an increase in the boundary layer thickness and in the shock wave angle when the flat plate surface is heated (see Figure 12). As the simulations are based on the experimental configuration of

the heater, the force calculations are therefore concentrated on the surface heating effect. The model studied is a beveled flat plate, so four domains are considered for the forces calculations in order to later distinguish the contribution of each domain (see Figure 13).

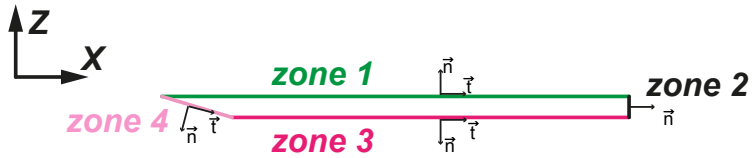

Figure 13. Domains considered for the force calculations from the numerical simulations.

The lift F_L and the drag F_D forces are calculated for each domain separately by integrating local pressure and shear stress along the total length of the flat plate. Thus, the equation that governs the forces is described by equation 9 and equation 10:

$$d\,\vec{F}_L = \left(-p\,\vec{n} + \tau\,\vec{t}\right) dl \tag{9}$$

according to the Z axis and

$$d\,\vec{F}_D = \left(-p\,\vec{n} + \tau\,\vec{t}\right) dl \tag{10}$$

according to the X axis,
where $\vec{n}$ is the vector normal to the surface, $\vec{t}$ is the vector tangential to the surface, p is the local pressure along dl and τ is the distribution of shear stresses along dl. The shear stress τ is deduced from the temperature distribution through the equation 11:

$$\tau = \mu \frac{dU}{dz}, \tag{11}$$

where U is the velocity of the fluid and μ is the viscosity based on the Sutherlands law (equation 12):

$$\mu = \frac{A\,T^{1.5}}{B + T}, \tag{12}$$

where T is the local temperature, and the two constants $A = 1.439 \times 10^{-6}\,\mathrm{Pa{\cdot}s{\cdot}K^{-0.5}}$ and $B = 110.56\,\mathrm{K}$ are related to air [29].

In order to have a standard for comparison, the lift and drag coefficients, C_L and C_D, respectively, are estimated (equation 13):

$$C_{L/D} = \frac{2F_{L/D}}{\rho_1 L\,U_1^2}, \tag{13}$$

where ρ_1 is the mass density of the fluid, U_1 is the flow velocity, and L is the reference length taken as the chord of the model (i.e., $L = 100\,\mathrm{mm}$).

Analysis

As the experimental studies of the shock wave angle were done according to the maximum wall temperature, this parameter $T_{w,max}$ is chosen to compare the different results obtained from the aerodynamic force calculations. To understand in a better way the behavior of the aerodynamic forces, Figures 14*a* and 14*b* show the variation of lift and drag forces according to $T_{w,max}$ for the different domains of the flat plate (zone 1, zone 3, and zone 4).

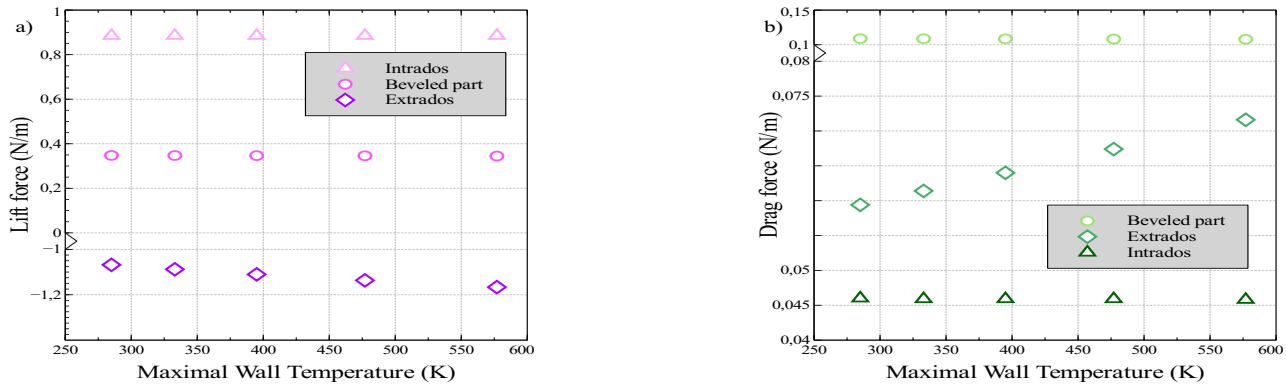

Figure 14. a) Lift force F_{L_i} of zone i and b) Drag force F_{D_i} of zone i, according to the maximum wall temperature in the case of the numerical simulations. The free stream Mach number is 2.

According to the experimental setup, the numerical code simulates a flat plate with no angle of attack. This, can explain that the aerodynamic forces had no real impact on the back of the model (zone 2). Therefore, this zone is not represented on the figures.

Figure 14*a* shows that the lift force on zone 1 (extrados) decreases strongly of quite 9% when the upper surface of the model is heated, while it remains constant on zone 3 and zone 4, which are located on the lower side of the flat plate. Figure 14*b* shows that the zone 4, corresponding to the beveled part of the model, contributes the most to the total drag of the model. On this particular part of the model, the viscous drag (caused by the shear stress) acts in addition to the pressure drag because of the geometry of this zone [30]. To be more precise, the pressure drag even accounts for quite 92% of the drag on this part. As for the lift force, the drag force increases only on zone 1 of almost 20% when the temperature of the upper surface of the model increases.

To determine global variations of the aerodynamic forces according to the maximum wall temperature, the sum of the different contributions for each part of the flat plate are plotted on Figure 15 for the lift and drag forces. It can be noticed that the lift force is decreasing when the temperature increases, whereas the drag force is expanding linearly. The absolute variation of the total drag is lower than the one of the total lift. This is due to the relative variation of F_{L_1} (the baseline is taken as the reference) that is several times higher than the relative variation of F_{D_1} (baseline as reference). These results are close to the ones obtained experimentally with a strain gauge in a previous study of our group [27], where it was observed that the model was undergoing a nose-up moment.

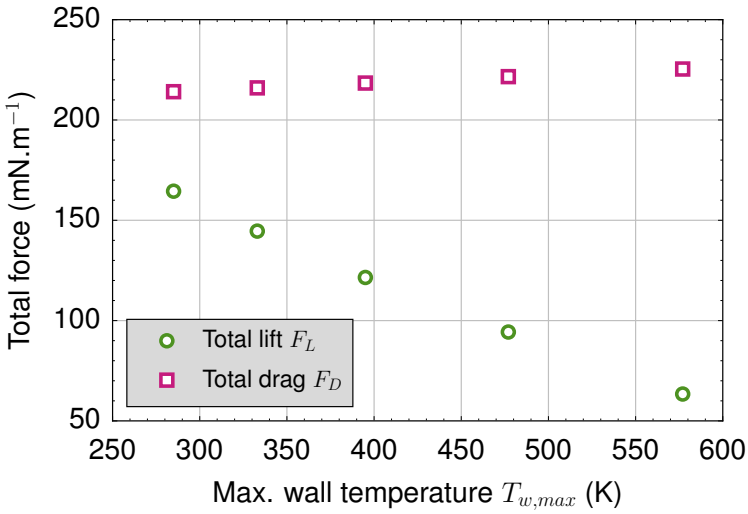

Figure 15. Lift and drag forces on the flat plate according to the maximum wall temperature in the case of the numerical simulations. The free stream Mach number is 2.

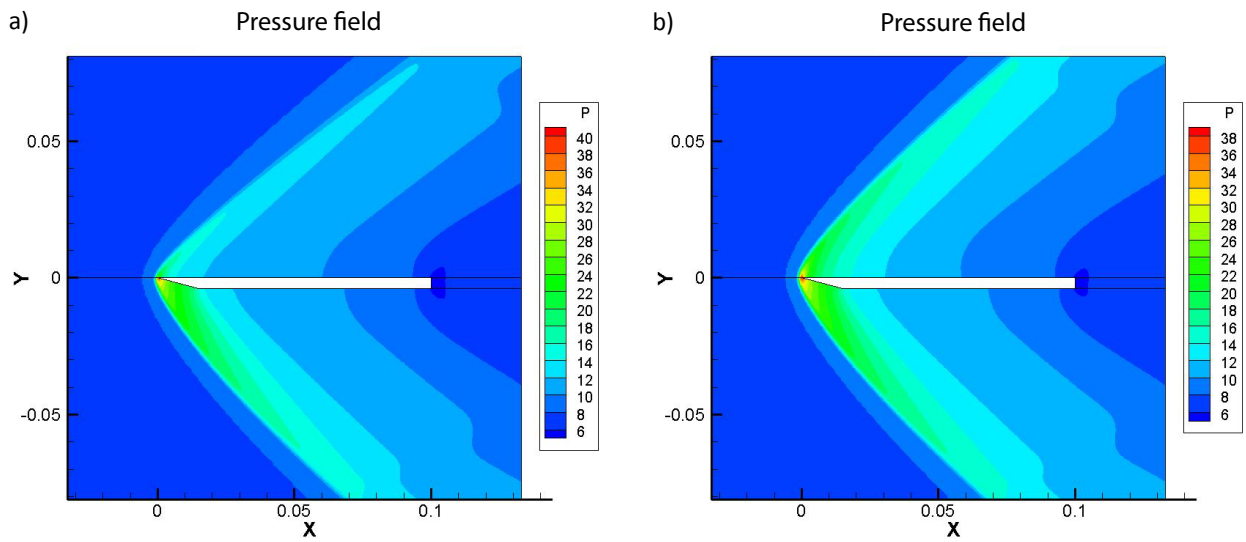

Figure 16. Local pressure fields obtained with the numerical results for two different maximum wall temperatures:a) $T_{w,max}$ = 284.5 K, and b) $T_{w,max}$ = 576.6 K.

It is possible to explain this observation by relying on the pressure flow field behavior with the wall temperature. Figure 16 shows two flow field maps of the local pressure calculated with to wall temperatures $T_{w,max} = 285K$ corresponding to the baseline case and $T_{w,max} = 577K$ corresponding to a hot walltemperature case. Comparing the two figures, it can be observed that the pressure distribution on the lowerpart of the model is slightly evolving compared to the extrados when heating the model. This can be explained by the fact that the lift force had a greater impact on the upper surface of the model than on the lower parts (see Figure 14*a*). However, the values of the pressures on the beveled part are greater than the ones on the extrados, therefore it confirms a nose-up moment.

From the results exposed in Figures 11 and 15, it is interesting to plot the variation of the aerodynamic coefficients according to the shock wave angle. Figures 17*a* and 17*b* show the variation of C_L and C_D estimated from the numerical simulations and the empirical law deduced from these calculations, respectively. The force coefficients C_L and C_D are linked to the shock wave angle β through the power law (equation 14):

$$C_{L/D} = a(\beta - \beta_{off})^n + C_{L_{off}/D_{off}}, \tag{14}$$

where a and n are two coefficients related to C_L or C_D (detailed in Table), and the subscript $_{off}$ corresponds to the initial condition (i.e., the baseline).

Table 2. Coefficients of empirical laws of aerodynamic coefficients (Eq. 14).

Aerodynamic coefficient	a	n
C_L	-1.17×10^{-2}	1.24
C_D	1.10×10^{-3}	1.40

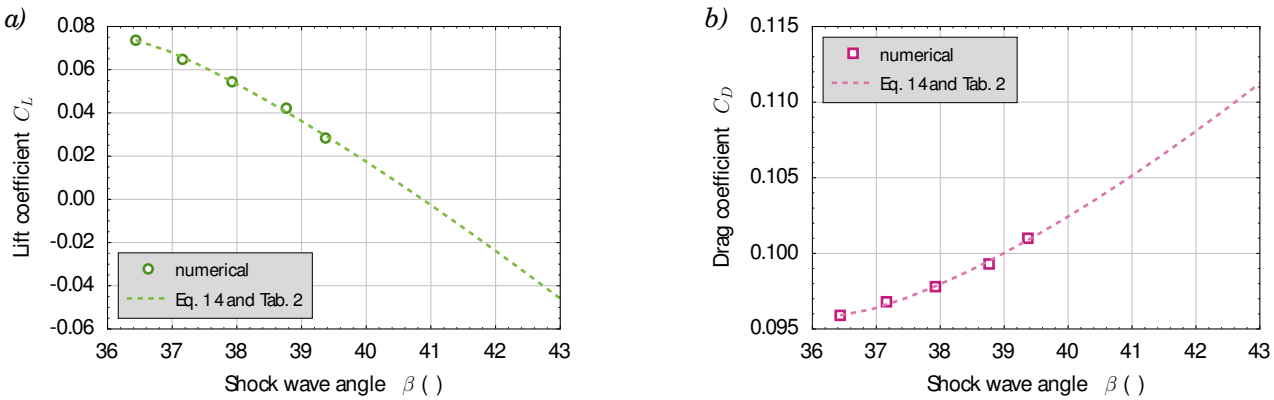

Figure 17. Aerodynamic coefficients obtained from the numerical simulations according to the shock wave angle: a) lift coefficient C_L, and b) drag coefficient C_D. The free stream Mach number is 2.

In order to get an estimation of the aerodynamic coefficients that would correspond to the plasma actuator, the empirical law, equation 14 is used to extrapolate the expected values of C_L and C_D in the case of the plasma actuator. This method allows to estimate the aerodynamic coefficients values correlated with the measured shock wave angles.

Knowing the relation between β and $T_{w,max}$ (from Figure 11), it is therefore possible to compare the variation of C_L and C_D between the plasma actuator (expected values) and the numerical simulations (calculated values), according to the maximal surface temperature (see Figure 18).

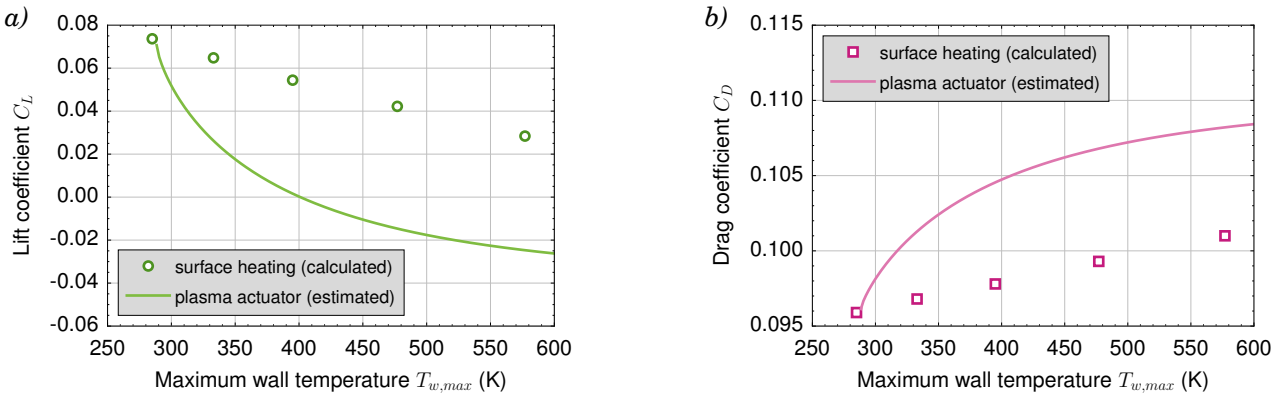

Figure 18. Aerodynamic coefficients obtained from the numerical simulations (purely surface heating, open symbols) and estimated for the plasma actuator (solid line) according to the maximum wall temperature: a) lift coefficient C_L, and b) drag coefficient C_D. The free stream Mach number is 2.

Figure 18 shows that the aerodynamic coefficients expected for the plasma actuator are higher (in terms of absolute value) than the ones calculated with a pure surface heating, for any surface temperature. For low values of Knudsen number, the wall temperature directly influences the viscosity and then the skin friction increases with the wall temperature. But when the Knudsen number increases, the influence of rarefied effects become important and the behavior of the skin friction becomes more complex because of the slip effects near the wall. [31] have calculated the effect of wall temperature of a flat plate on aerodynamics properties and shown that for Knudsen number larger than 0.01, the total drag increases with the wall temperature, as observed in this investigation. When the Knudsen number is larger than 1, the total drag decreases. Nevertheless, the corresponding Knudsen number at which the trend of the total drag changes depends on the Mach number.

The discussion is focused on the drag force because during atmospheric re-entries, it is directly linked with deceleration. In terms of relative variation, for a maximum wall temperature increase of almost 50%, C_D is modified by +13.0% for the plasma actuation, in comparison to +5% for a pure surface heating (i.e., the numerical simulations). In addition, one can notice that for $T_{w,max} > 400$ K, the lift coefficient goes in the negative values. This result is due to the fact that in this investigation the flat plate has no incidence angle with respect to the free stream direction.

As the main goal is to decrease the speed of a spaceship, in view to decrease the total heat, it is interesting to study the effect of the drag diminution on the heat flux over the spaceship. For the re-entry of the space Shuttle , an increase of 13% of the total drag, as estimated in this paper, corresponds to a decrease in the vehicle speed of about 7% [32] and of about 26% of the heat flow because the heat flow is proportional to the power 3.15 of speed.
Taking into account that the mass of the heat protection in the Shuttle is of 9575 kg and that the decrease of the heat flow is proportional to the mass protection [33], 2.5 tons of the Shuttle mass could be saved with the plasma actuator.

Conclusions

In this study, it is experimentally observed that the plasma actuator induces an increase in the shock wave angle. A comparison with the heating element showed that the effect of the plasma actuator is greater. It demonstrates that other types of effects than thermal ones are involved.

Numerical simulations are performed with a Navier-Stokes code adapted with slip boundary conditions to rarefied flow regime. In addition, to reproduce the surface heating measured experimentally, the boundary condition of the upper surface of the flat plate are modified. Different temperature distributions are tested and agree with real experimental cases.

Based on these simulations, the lift and drag forces are evaluated. The heating of the flat plate surface increases the drag force. Thus, this work is in good agreement with the aim to increase drag and therefore, to slow down the spacecraft in the context of atmospheric re-entries. In order to confirm the values estimated numerically in the present work, a wind tunnel balance will be developed to measure drag and lift forces applied to the flat plate equipped with the plasma actuator.

Acknowledgements

Romain Joussot's fellowship is provided by the French Government's Investissement d'Avenir program: Laboratoire d'Excellence CAPRYSSES (grant no. ANR-11-LABX-0006-01). Additional funding is provided by the Région Centre with the PASS grant (convention no. 00078782).
The authors would furthermore like to acknowledge the constructive feedback from the reviewers.

References

References

[1] BAKHTIAN, NM and AFTOSMIS, MJ (2011). *Maximum attainable drag limits for atmospheric entry via supersonic retropropulsion*. In: 8th. International Planetary Probe Workshop, Porstmouth, Virginia, USA.

[2] ELIAS, P.-Q and CHANETZ, B and LARIGALDIE, S and PACKAN, D (2007). *Study of the effect of glow discharges near a M = 3 bow shock*. In: AIAA Journal, vol. 45, pp. 2237-2245.

[3] SHIN, J and NARAYANASWAMY, V and RAJA, LL and CLEMENS NT (2007). *Characterization of a Direct-Current Glow Discharge Plasma Actuator in Low-Pressure Supersonic Flow*. In: AIAA Journal, vol. 45, pp. 1596-1605.

[4] SURZHIKOV, ST and SHANG, J (2014). *Normal glow discharge in axial magnetic field*. In: Plasma Sources Science and Technologie, vol. 23, p.054017.

[5] PALM, P and MEYER, R and PL-OGRAVE, E and RICH, JW and ADAMOVITCH, IV (2003). *Nonequilibrium radio frequency discharge plasma effect on conical shock wave: M= 2.5 flow*. In: AIAA journal, vol.41.

[6] LAGO, V and JOUSOT, R and PARISSE, J.-D (2014). *Influence of the ionization rate of a plasma discharge applied to the modification of a supersonic low Reynolds number flow field around a cylinder*. In: Journal of Physics D: Applied Physics, vol.47.

[7] WANG, J and LI, Y and XING, F (2014). *Investigation on oblique shock wave control by arc discharge plasma in supersonic airflow*. In: Journal of Physics D: Applied Physics, vol.47.

[8] PARISSE, J.-D and LÉGER, L and DEPUSSAY, E and LAGO, V and BURTSCHELL, Y (2009). *Comparison between Mach 2 rarefied airflow modification by an electrical discharge and numerical simulation of airflow modification by surface heating*. In: Physics of Fluids (1994-present), vol. 21, pp. 103-106.

[9] GAD-EL-HAK, M (1999). *The fluid mechanics of microdevices-the freeman scholar lecture*. In: Transactions-American Society of Mechanical Engineers Journal of FLUIDS Engineering, vol. 121, pp. 5-33.

[10] CHUE, SH (1975). *Pressure probes for fluid measurement*. In: Progress in aerospace sciences, vol. 16, pp. 147-223.

[11] BRUN, R (2012). *High Temperature Phenomena in Shock Waves*. In: Springer Science & Business Media, ch. 7.

[12] FISHER, S and BHARATHAN, D (1973). *Glow-discharge flow visualization in low-density free jets*. In: Journal of Spacecraft and Rockets, vol. 10, pp. 658-662.

[13] LOFTHOUSE, AJ and SCALABRIN, LC and BOYD, ID (2008). *Velocity slip and temperature jump in hypersonic aerothermodynamics*. In: Journal of thermophysics and heat transfer, vol. 22, pp. 38-49.

[14] HIRSCHFELDER, JO and CURTISS, CF and BIRD, RB and MAYER, MG (1954). *Molecular theory of gases and liquids*. In: Wiley New York, vol. 26.

[15] KOGAN, MN (1967). *Dynamics of rarefied gas*. In: Kinetic Theory.

[16] SHARIPOV, F (2004). *Data on the velocity slip and temperature jump coefficients [gas mass, heat and momentum transfer]*. In: Thermal and Mechanical Simulation and Experiments in Microelectronics and Microsystems, 2004. EuroSimE 2004. Proceedings of the 5th International Conference on, pp. 243-249.

[17] PARISSE, J.-D and KUDRYAVTSEV, AN and LAGO, V (2015). *Mach 2 rarefied airflow over a plate submitted to a DC discharge: surface temperature gradient investigation*. In: International Journal of Engineering Systems Modelling and Simulation, vol. 7, pp. 271-278.

[18] SMOLUCHOWSKI, von M (1898). *Uber Warmeleitungen in verdünnten gasen*. In: Ann. Phys. Chem, pp. 101-130.

[19] SHARIPOV, F (2003). *Application of the Cercignani–Lampis scattering kernel to calculations of rarefied gas flows. II. Slip and jump coefficients*. In: European Journal of Mechanics-B/Fluids, vol. 22, pp. 133-143.

[20] BIRD, GA (1994). *Molecular gas dynamics and the direct simulation of gas flows*. In: Clarendon Press.

[21] DONAT, R and MARQUINA, A (1996). *Capturing shock reflections: an improved flux formula*. In: Journal of Computational Physics, vol. 125, pp. 42-58.

[22] MARKELOV, GN and KUDRYAVTSEV, AN and IVANOV, MS (2000). *Continuum and kinetic simulation of laminar separated flow at hypersonic speeds*. In: Journal of spacecraft and rockets, vol. 37, pp. 499-506.

[23] RAIZER, P (1991). *Gas discharge physics*. In: Berlin: Springer.

[24] MENIER, E and LEGER, L and DEPUSSAY, E and LAGO, V and ARTANA, G (2007). *Effect of a dc discharge on the supersonic rarefied air flow over a flat plate*. In: Journal of Physics D: Applied Physics, vol. 40, p.695.

[25] HAYES, WD (1966). *Hypersonic flow theory*, vol. 1: inviscid flows.

[26] MENART, J and HENDERSON, S and ATZBACH, C and SHANG, J and KIMMEL, R and HAYES, J (2004). *Study of surface and volumetric heating effects in a Mach 5 flow*. In: 35th AIAA Plasmadynamics and Lasers Conference, pp. 1-2.

[27] MENIER, E (2007). *Influence d'une décharge électrique continue sur un écoulement supersonique raréfié*. PhD thesis. University of Orléans.

[28] JOUSSOT, R and LAGO, V and PARISSE, J.-D (2015). *Quantification of the effect of surface heating on shock wave modification by a plasma actuator in a low-density supersonic flow over a flat plate*. In: Experiments in Fluids, vol. 56, pp. 1-18.

[29] REID, RC and PRAUSNITZ, JM and POLING, BE (1987). *The properties of gases and liquids*. In: McGraw Hill Book Co., New York, NY.

[30] KOPPENWALLNER, G (1985). *The drag of simple shaped bodies in the rarefied hypersonic flow regime*. In: AIAA-85, vol. 998.

[31] HU, Y and CHEN, S and SUN, Q (2012). *Hypersonic aerodynamics of a flat plate: Bridging formula and wall temperature effects*. In: AMER INST PHYSICS

[32] HALE, W and CHAPLINE, G (2010). *Wings In Orbit*. In: Education, vol. 9, p.20.

[33] BOLONKIN, AA (2006). *A new method of atmospheric reentry for space shuttle*. In: AIAA Conference, pp. 6-9.